Optical Network Analysis and Longitudinal Structure Characterization of Fiber Bragg Grating

David Sandel, Reinhold Noé, G. Heise, and B. Borchert

Abstract— **A method for polarization-resolved optical fiber Bragg grating (FBG) characterization is reported on. The complete reflectance Jones matrix is measured interferometrically. Required polarization transformers need not be accurate, just to operate reproducibly, because redundant measurements yield pairs of orthogonal polarizations. Local dichroic reflectivity and birefringence of a sampled grating was derived from this data. Knowledge of these quantities should allow improvement of the ultraviolet (UV) illumination process and to effectively correct phase mask errors by longitudinally selective UV light postprocessing.**

Index Terms— **Birefringence, Bragg scattering, gratings, inverse problems, optical interferometry, optical polarization, scattering parameters measurement.**

I. INTRODUCTION

FIBER Bragg gratings (FBG's) [1] are finding applications in optical transmission technology. Of great interest are chirped gratings for dispersion compensation [2]–[4], but these require highest fabrication accuracy. For unrestricted, polarization-insensitive operation not only the desired refractive index modulation must be met precisely, but the grating must also be free of birefringence [5] and dichroism. The fabrication process has, therefore, to be optimized in all these respects.

We will see that optical network analysis, the analogon of electrical network analysis, is suitable for characterizing gratings during and after fabrication. A number of activities have been reported concerning optical network analysis.

Noninterferometric methods rely on modulation. In fact, any direct detection experiment with analog intensity modulation and an electrical network analyzer connected to transmitter input and receiver output yields an electrical transfer function from which optical transfer function magnitude and group delay are obtained. This scheme may be expanded to include different polarizations [6]. Anyway, sensitivity is limited due to the direct-detection process. The phase of the optical transfer function is only accessible by way of integrating the group delay over frequency. This limits accuracy, and does not allow for determining the correct phase relationship between transfer functions obtained from different polarizations.

Interferometric measurement with fixed polarizations [7]–[9] is the simplest, one-port form of optical network

analysis. Low-coherence interferometry [7] in particular directly yields the impulse response of a device with an excellent $\sim$100 μm spatial resolution. In contrast, frequency-domain interferometry [9], which is also being used in this work, gives a frequency-dependent reflection factor (reflectance) from which the impulse response may be calculated. Spatial resolution is limited by the laser tuning range, but large grating lengths may be investigated due to the high coherence of a singlemode laser. In any case, the impulse response allows to determine the structure of an isotropic grating [8], [10]. The knowledge of refractive index modulation depth and phase should allow for a correction of aberrations from the desired structure by local ultraviolet (UV) light postprocessing [10].

In the following, we first derive both dichroic reflectivity and fiber birefringence along the grating from given network analysis data [11]–[14] (Section II), then describe how an optical network analyzer can be setup without calibrated polarization transformers (Section III). These algorithms have been used experimentally to characterize a sampled FBG (Section IV). We hope the results will eventually allow for improvement of the fabrication accuracy of gratings.

II. CALCULATION OF REFRACTIVE INDEX MATRIX

The refractive index matrix in a lossy grating may be written as

$$\mathbf{n}(z) = \bar{n}\big(1 + \omega_0^{-1}(\beta(z) + j\gamma(z) + 2\operatorname{Re}(-je^{j2(\omega_0/c)\bar{n}z}\kappa(z)))\big) \tag{1}$$

where ω_0 is a fixed optical angular center frequency, $\bar{n}$ a mean refractive index assumed to be constant, c the speed of light, and z the longitudinal position. The coupling matrix

$$\kappa(z) = j\frac{\omega_0}{4\bar{n}}e^{-j\phi(z)}\begin{bmatrix} \Delta n_{pp11}(z) & \Delta n_{pp12}(z) \\ \Delta n_{pp12}^*(z) & \Delta n_{pp22}(z) \end{bmatrix} = \mathbf{E}_\kappa \mathbf{\Lambda}_\kappa \mathbf{E}_\kappa^+ \tag{2}$$

with

$$\mathbf{\Lambda}_\kappa = \begin{bmatrix} \kappa_1 & 0 \\ 0 & \kappa_2 \end{bmatrix} \quad \arg(\kappa_1) = \arg(\kappa_2) \tag{3}$$

represents grating reflectivity which behaves like a retardation-free partial polarizer. A hermitian matrix with peak-to-peak refractive index modulation amplitudes $\Delta n_{ppik}(z)$ is preceded by a phasor containing the mean reflection or grating phase $\phi(z)$. Diagonalization of (2) yields two complex eigenvalues κ_1, κ_2 with equal phase angles (3 unknowns), and complex orthogonal eigenmodes (2 unknowns) which form a unitary

eigenvector matrix $\mathbf{E}_\kappa$. The hermitian conjugate (superscript "+") may therefore be used instead of the matrix inverse. The birefringence matrix

$$\beta(z) = \frac{\omega_0}{\bar{n}} \begin{bmatrix} \Delta n_{11}(z) & \Delta n_{12}(z) \\ \Delta n_{12}^*(z) & -\Delta n_{11}(z) \end{bmatrix} = \mathbf{E}_\beta \begin{bmatrix} \beta & 0 \\ 0 & -\beta \end{bmatrix} \mathbf{E}_\beta^+ \quad (4)$$

represents a lossless retarder with refractive index differences $\Delta n_{ik}(z)$. This special hermitian matrix has real eigenvalues $\pm\beta$ the sum of which equals zero (one unknown) and complex orthogonal eigenmodes (two unknowns) which form a unitary eigenvector matrix $\mathbf{E}_\beta$. The hermitian gain (or negative attenuation) matrix

$$\gamma = \mathbf{E}_\gamma \begin{bmatrix} \gamma_1 & 0 \\ 0 & \gamma_2 \end{bmatrix} \mathbf{E}_\gamma^+ \quad (5)$$

is assumed to be known and has been included here for the purpose of allowing for modeling constant background loss. It has real eigenvalues γ_1, γ_2 and again a unitary eigenvector matrix, $\mathbf{E}_\gamma$.

κ, β and γ vary slowly with position z. The eight real unknowns in κ and β are balanced by the four complex elements of the 2×2 grating reflectance matrix

$$\rho(f) = \begin{bmatrix} \rho(f)_{r_\parallel, t_\parallel} & \rho(f)_{r_\parallel, t_\perp} \\ \rho(f)_{r_\perp, t_\parallel} & \rho(f)_{r_\perp, t_\perp} \end{bmatrix}. \quad (6)$$

Subsubscripts $\parallel$ and $\perp$ refer to pairs of orthogonal polarizations, both at the input of the device under test and as reference analyzed at its output (subscripts t, r). For grating structure characterization, the matrix impulse response

$$\mathbf{U}(0, t) = \begin{bmatrix} U(0, t)_{r_\parallel, t_\parallel} & U(0, t)_{r_\parallel, t_\perp} \\ U(0, t)_{r_\perp, t_\parallel} & U(0, t)_{r_\perp, t_\perp} \end{bmatrix} \quad (7)$$

is calculated by inverse Fourier transform of each of the reflectances

$$U(0, t)_{r_i, t_k} = F^{-1}\big(\rho(f)_{r_i, t_k}\big). \quad (8)$$

The column vectors of $\mathbf{U}(0, t)$ represent the causal envelope vectors reflected at position $z = 0$ for orthogonally polarized cartesian envelope vectors $\begin{bmatrix} 1 \\ 0 \end{bmatrix}\delta(t)$ and $\begin{bmatrix} 0 \\ 1 \end{bmatrix}\delta(t)$, respectively, incident at the grating input $z = 0$. Abstractly speaking, $\mathbf{U}(0, t)$ may be considered to be the impulse response to $\mathbf{D}(0, t) = \mathbf{1}\delta(t)$, a Dirac impulse unity matrix.

More generally, propagation of the wave envelopes in time (t) and one-dimensional (1-D) space (z) is governed by the coupled differential equations

$$\left(c/\bar{n}\frac{\partial}{\partial z} + \frac{\partial}{\partial t}\right)\mathbf{D}(z, t) = (-j\beta(z) + \gamma(z))\mathbf{D}(z, t)$$
$$+ \kappa^+(z)\mathbf{U}(z, t)$$
$$\left(c/\bar{n}\frac{\partial}{\partial z} - \frac{\partial}{\partial t}\right)\mathbf{U}(z, t) = (j\beta(z) - \gamma(z))\mathbf{U}(z, t)$$
$$+ \kappa(z)\mathbf{D}(z, t) \quad (9)$$

where $\mathbf{D}$ is the electric field matrix of the forward-, and $\mathbf{U}$ the matrix of the backward-propagating wave. In order to calculate $\kappa(z)$ and $\beta(z)$ we discretize (9), using a position step Δz and a corresponding time step $\Delta t = \frac{\bar{n}}{c}\Delta z$.
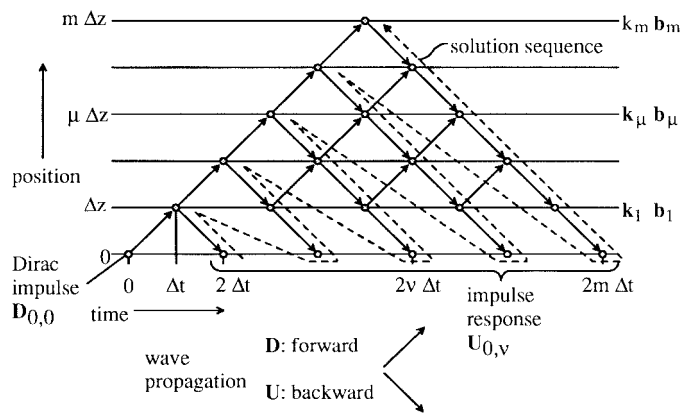
Fig. 1. Wave propagation and solution sequence.

A pair of discrete equations

$$\mathbf{U}_{\mu,\nu} = \tau_{\mu-1}^{-1}\big(\mathbf{b}_{\mu-1}^{-1}\mathbf{g}_{\mu-1}^{-1}\mathbf{U}_{\mu-1,\nu+1}$$
$$+ \mathbf{k}_{\mu-1}\mathbf{g}_{\mu-1}\mathbf{b}_{\mu-1}\mathbf{D}_{\mu-1,\nu+1}\big)$$
$$\mathbf{D}_{\mu,\nu} = \tau_{\mu-1}^{-1}\big(-\mathbf{k}_{\mu-1}^+\mathbf{b}_{\mu-1}^{-1}\mathbf{g}_{\mu-1}^{-1}\mathbf{U}_{\mu-1,\nu-1}$$
$$+ \mathbf{g}_{\mu-1}\mathbf{b}_{\mu-1}\mathbf{D}_{\mu-1,\nu-1}\big) \quad (10)$$

is derived from piecewise solutions of (9) under the assumption of locally constant κ, β, γ. Matrices

$$\mathbf{k} = \kappa\Delta z = \mathbf{E}_\kappa \begin{bmatrix} \kappa_1\Delta z & 0 \\ 0 & \kappa_2\Delta z \end{bmatrix} \mathbf{E}_\kappa^+ = \mathbf{E}_\kappa \begin{bmatrix} k_1 & 0 \\ 0 & k_2 \end{bmatrix} \mathbf{E}_\kappa^+$$
$$(11)$$

$$\mathbf{b} = \exp(-j\beta\Delta z) = \mathbf{E}_\beta \begin{bmatrix} \exp(-j\beta\Delta z) & 0 \\ 0 & \exp(j\beta\Delta z) \end{bmatrix} \mathbf{E}_\beta^+$$
$$= \mathbf{E}_\beta \begin{bmatrix} b & 0 \\ 0 & b^* \end{bmatrix} \mathbf{E}_\beta^+ \quad (12)$$

$$\mathbf{g} = \exp(\gamma\Delta z) = \mathbf{E}_\gamma \begin{bmatrix} \exp(\gamma_1\Delta z) & 0 \\ 0 & \exp(\gamma_2\Delta z) \end{bmatrix} \mathbf{E}_\gamma^+ \quad (13)$$

cover coupling, birefringence and gain (inverse loss), respectively, of one position step, and are given in diagonalized forms here. Transmission matrix τ must satisfy the losslessness relation

$$\tau^+\tau + \mathbf{k}^+\mathbf{k} = 1. \quad (14)$$

It is hermitian and has the same eigenmodes as $\mathbf{k}$. In the calculation

$$\tau = \sqrt{1 - \mathbf{k}^+\mathbf{k}} = \mathbf{E}_\kappa \begin{bmatrix} t_1 & 0 \\ 0 & t_2 \end{bmatrix} \mathbf{E}_\kappa^+ \quad (t_1, t_2 > 0) \quad (15)$$

positive signs must be chosen for its real eigenvalues t_1, t_2.

Fig. 1 shows wave propagation and solution sequence in a grid of time and space. Solution starts from the knowledge of the incident unity matrix $\mathbf{D}_{0,0}$ (the only nonzero component of a discretized $\mathbf{D}(0, t) = \mathbf{1}\delta(t)$) and the measured impulse response matrix $\mathbf{U}_{0,\nu}$ (discretized $\mathbf{U}(0, t)$). Waves $\mathbf{D}_{\mu,\nu}$, $\mathbf{U}_{\mu,\nu}$ and, as far as yet unknown, matrices $\mathbf{k}$ and $\mathbf{b}$ are calculated in a sequence given by the dashed arrow.

Mathematically speaking, for calculation of $\mathbf{k}_m$ and $\mathbf{b}_m$ all $\mathbf{k}_\mu$, $\mathbf{b}_\mu$, γ_μ, and τ_μ with $0 < \mu < m$ must be known. This is automatically the case if one starts with $m = 1$. Each

solution step then requires (10) to be solved successively for $\mu = 1 \cdots m$, $\nu = 2m - \mu$. $\mathbf{D}_{m,m}$ and $\mathbf{U}_{m,m}$ are obtained as an intermediate result. Their matrix quotient

$$\mathbf{Q}_m := -\mathbf{U}_{m,m}\mathbf{D}_{m,m}^{-1} = \mathbf{b}_m \mathbf{k}_m \mathbf{b}_m \qquad (16)$$

has to be decomposed into the product of a partial polarizer matrix $\mathbf{k}_m$ and two lossless retarder matrices $\mathbf{b}_m$ as shown on the right side of (16). First, the product

$$\mathbf{Q}^+ \mathbf{Q} = (\mathbf{bkb})^+ \mathbf{bkb} = \mathbf{b}^+ \mathbf{E}_\kappa \mathbf{\Lambda_k^+} \mathbf{\Lambda_k} \mathbf{E}_\kappa^+ \mathbf{b} \qquad (17)$$

delivers $|k_1|$, $|k_2|$ as the square roots of its eigenvalues. The missing argument is

$$\arg(k_1) = \arg(k_2)$$
$$= \frac{1}{2} \arg(\det(\mathbf{k})) \quad \text{or} \quad \frac{1}{2} \arg(\det(\mathbf{k})) + \pi. \qquad (18)$$

Second, the eigenvector matrix $(\mathbf{b}^+ \mathbf{E}_\kappa)$ of (17) allows for the calculation of the matrix

$$(\mathbf{bE}_\kappa) = \mathbf{Q}(\mathbf{b}^+ \mathbf{E}_\kappa)\mathbf{\Lambda_k^{-1}}. \qquad (19)$$

Third, we obtain

$$(\mathbf{b}^2) = (\mathbf{bE}_\kappa)(\mathbf{E}_\kappa^+ \mathbf{b}) \qquad (20)$$

which successively leads to

$$\mathbf{b} = \sqrt{(\mathbf{b}^2)} \qquad (21)$$
$$\mathbf{E}_\kappa = \mathbf{b}^+(\mathbf{bE}_\kappa) \qquad (22)$$
$$\mathbf{k} = \mathbf{E}_\kappa \mathbf{\Lambda}_\kappa \mathbf{E}_\kappa^+. \qquad (23)$$

Ambiguities in (18), (21) have to be settled so that $\mathbf{b}$ has the smallest possible eigenvalue arguments. Otherwise $|\beta|$ would approach infinity for vanishing Δz.

Finally, local grating birefringence

$$\beta = j \frac{\ln(\mathbf{b})}{\Delta z} = \frac{1}{\Delta z} \mathbf{E}_\beta \begin{bmatrix} -\arg(b) & 0 \\ 0 & \arg(b) \end{bmatrix} \mathbf{E}_\beta^+ \qquad (24)$$

and local coupling strength

$$\kappa = \frac{\mathbf{k}}{\Delta z} \qquad (25)$$

are calculated. Comparison with (2), (4) yields grating refractive index modulation amplitudes $\Delta n_{pp\,ik}$, grating phase ϕ, and refractive index differences Δn_{ik} for birefringence.

The matrices $\mathbf{k}$, $\mathbf{b}$, τ (15) are now ready to be used in (10) for further solution steps until the complete grating structure is obtained. Matrix $\mathbf{g}$ must likewise be known. Obvious choices are no or constant background loss. However, a loss proportional to the mean local coupling factor or any other assumed dependence of $\mathbf{g}$ on the just-calculated matrices $\mathbf{k}$, $\mathbf{b}$ can also be applied.

Fig. 2 summarizes the full, polarization-resolved grating characterization procedure undertaken in this work. Some more details will be explained in Sections III and IV.

Circular birefringence merits special attention. In (4) it is characterized by vanishing Δn_{11} and imaginary Δn_{12}. In a lossless medium, this means the three-dimensional (3-D) dielectricity tensor ε has imaginary off-diagonal elements
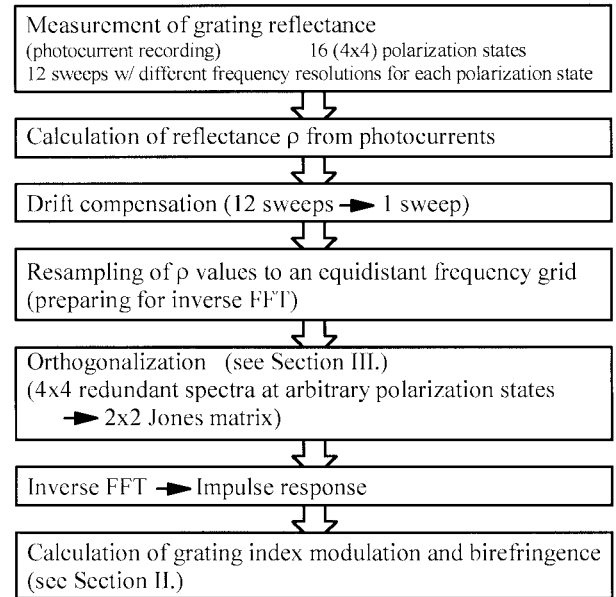
Fig. 2. Summary of grating characterization procedure.

and is hermitian. Such a medium is nonreciprocal because reciprocity would require a symmetric ε. As a consequence, the circular birefringence determined by our algorithm is nonreciprocal like the Faraday rotation.

However, fiber twist causes reciprocal circular birefringence of photoelastic origin just like any chiral molecule (optical activity). From the above it may be concluded that fiber twist can not be described macroscopically by a single dielectricity tensor that is valid for both propagation directions along the twist axis. Fortunately, reciprocal circular birefringence as a single effect in an otherwise isotropic reflecting device cancels in forward and backward directions. But the coordinate system which in the general case defines both linear birefringence and linear reflection dichroicity rotates along the fiber according to reciprocal circular birefringence. This rotation is ~0.08 times the actual twist angle [15]. Unknown twist will therefore falsify the coordinate system of linear birefringence and linear reflection dichroicity.

For the purpose of optimizing grating performance fiber twist is not expected to be a big issue. Only if one intended to create specific linear birefringence or reflection dichroicity one would have to apply a small test quantity thereof in order to determine the local orientation. If the goal is simply to optimize fabrication conditions such that an isotropic grating is created automatically, then the detection of birefringence (with the exception of circular reciprocal birefringence) and reflection dichroism is sufficient, and this is always possible. Anyway, mechanical relaxation of a fiber piece with loose ends should normally eliminate twist.

III. POLARIZATION ORTHOGONALIZATION

The 2×2 grating reflectance matrix (6) can be measured interferometrically. However, depending on available apparatus it may be difficult to generate the required orthogonal polarization pairs without breaking or moving optical fiber. In order to be able to use uncalibrated polarization transformers

in a fiber-optic interferometer, a polarization orthogonalization procedure is derived in the following.

A birefringent or dichroic optical device, e.g., an FBG, has a reflection factor $\rho = \rho(f)$ which depends on input and analyzed output polarizations. An interferometric measurement determines a complex reflection factor (reflectance)

$$\rho_{r,t} = \mathbf{E}_r^+ \rho \mathbf{E}_t \qquad (26)$$

where $\mathbf{E}_r$ is the Jones vector in the reference branch, and $\mathbf{E}_t$ the Jones vector at the device under test. Only copolarized wave components interfere.

In order to determine the complete reflectance matrix ρ, a 2×2 Jones matrix, four factors $\rho_{r,t}$ have to be measured, and these will be the elements of ρ if $\mathbf{E}_r$, $\mathbf{E}_t$ are two pairs of cartesian unit vectors. If $\mathbf{E}_r$, $\mathbf{E}_t$ are unknown but orthogonal pairs, $\rho_{r,t}$ are the elements of a transformed ρ that has been multiplied by unitary matrices $[\mathbf{E}_{r_\parallel}, \mathbf{E}_{r_\perp}]^+$, $[\mathbf{E}_{t_\parallel}, \mathbf{E}_{t_\perp}]$ from left and right, respectively. Knowledge of the transformed ρ is generally sufficient because it reveals dichroism, and differential group delay between principal states of polarization.

When orthogonal polarization pairs are not available the transformed elements $\rho_{r,t}$ corresponding to orthogonal pairs of $\mathbf{E}_r$ and $\mathbf{E}_t$ can be deduced from 16 reflectances

$$\rho_{r_i,t_k} \quad i,k \in \{0 \cdots 3\} \qquad (27)$$

measured with four arbitrary $\mathbf{E}_{r_i}$ and four arbitrary $\mathbf{E}_{t_k}$. Polarization transformers which generate these waves must operate reproducibly but calibration is not needed. Elements $\rho_{r,t}$ corresponding to orthogonal pairs of $\mathbf{E}_r$ and $\mathbf{E}_t$ can be derived from ρ_{r_i,t_k}. Special cases excluded, every $\mathbf{E}_{t_k}$ can be expressed by a linear combination of any two others, for example

$$\mathbf{E}_{t_0} = \zeta_1 \mathbf{E}_{t_1} + \zeta_2 \mathbf{E}_{t_2} = \vartheta_1 \mathbf{E}_{t_1} + \vartheta_3 \mathbf{E}_{t_3}. \qquad (28)$$

For fixed i the reflectances can be expressed using the same coefficients

$$\rho_{r_i,t_0} = \zeta_1 \rho_{r_i,t_1} + \zeta_2 \rho_{r_i,t_2} = \vartheta_1 \rho_{r_i,t_1} + \vartheta_3 \rho_{r_i,t_3}. \qquad (29)$$

Factors ζ_1, ζ_2, ϑ_1, ϑ_3 are determined by measurement using (29).

Every $\mathbf{E}_{t_k}$ can further be expressed by the desired orthogonal pair $\mathbf{E}_{t_\parallel}$, $\mathbf{E}_{t_\perp}$ as

$$\mathbf{E}_{t_k} = C_k \mathbf{E}_{t_\parallel} + D_k \mathbf{E}_{t_\perp} \quad (|C_k|^2 + |D_k|^2 = 1, \quad k = 1 \cdots 3). \qquad (30)$$

For $k = 0$ let $\mathbf{E}_{t_0} = \mathbf{E}_{t_\parallel}$ by definition. There are nine degrees-of-freedom (DOF) in C_k, D_k. The eight real equations in (28) balance them except for the phase of one component of $\mathbf{E}_{t_\perp}$, which can be freely chosen. For example, D_1 can be set to be a positive real.

For the $\mathbf{E}_{t_\parallel}$ and $\mathbf{E}_{t_\perp}$ polarization components the insertion of (30) into (28) results in

$$1 = \zeta_1 C_1 + \zeta_2 C_2 \quad 1 = \vartheta_1 C_1 + \vartheta_3 C_3 \qquad (31)$$

and

$$0 = \zeta_1 D_1 + \zeta_2 D_2 \quad 0 = \vartheta_1 D_1 + \vartheta_3 D_3 \qquad (32)$$

respectively. This allows the expression of C_2, C_3, D_2, D_3 by C_1, D_1

$$C_2 = \frac{1 - \zeta_1 C_1}{\zeta_2} \quad C_3 = \frac{1 - \vartheta_1 C_1}{\vartheta_3} \qquad (33)$$

$$D_2 = -\frac{\zeta_1}{\zeta_2} D_1 \quad D_3 = -\frac{\vartheta_1}{\vartheta_3} D_1. \qquad (34)$$

The expressions $|C_k|^2 + |D_k|^2 = 1$ $(k = 1 \cdots 3)$, with (33), (34) inserted for $k = 2, 3$, lead to a set of two equations linear in $\mathrm{Re}(C_1)$ and $\mathrm{Im}(C_1)$. The solution is

$$\begin{bmatrix} \mathrm{Re}(C_1) \\ \mathrm{Im}(C_1) \end{bmatrix} = \frac{1}{2} \begin{bmatrix} \mathrm{Re}(\vartheta_1) & -\mathrm{Im}(\vartheta_1) \\ \mathrm{Re}(\zeta_1) & -\mathrm{Im}(\zeta_1) \end{bmatrix}^{-1} \begin{bmatrix} 1 - |\zeta_2|^2 + |\zeta_1|^2 \\ 1 - |\vartheta_3|^2 + |\vartheta_1|^2 \end{bmatrix}. \qquad (35)$$

The positive real factor D_1 can be derived from C_1

$$D_1 = \sqrt{1 - |C_1|^2}. \qquad (36)$$

C_1 and D_1 are in principle sufficient to calculate $\mathbf{E}_{t_\perp}$ from $\mathbf{E}_{t_0}$ and $\mathbf{E}_{t_1}$ and the corresponding reflection factors

$$\mathbf{E}_{t_\perp} = \frac{\mathbf{E}_{t_k} - C_k \mathbf{E}_{t_0}}{D_k} \quad \rho_{r_i,t_\perp} = \frac{\rho_{r_i,t_k} - C_k \rho_{r_i,t_0}}{D_k}$$
$$(i = 0 \cdots 3, k = 1) \quad (37)$$

In practice there are random errors in every measured $\rho_{r',t'}$. These lead to errors in $\rho_{r_i,t_\perp}$, which are enhanced by the factor $1/D_1$. Since C_2, C_3, D_2, D_3 are easily derived from C_1 and D_1 using (33), (34), the index $k = 1$ in (37) may be replaced by $k = 2, 3$, or an average over all $k = 1 \cdots 3$ is taken which may be a better choice. $|D_k|^2$-weighted averages

$$\mathbf{E}_{t_\perp} = \frac{\sum_{k=1}^3 |D_k|^2 \frac{\mathbf{E}_{t_k} - C_k \mathbf{E}_{t_0}}{D_k}}{\sum_{k=1}^3 |D_k|^2}$$
$$\rho_{r_i,t_\perp} = \frac{\sum_{k=1}^3 |D_k|^2 \frac{\rho_{r_i,t_k} - C_k \rho_{r_i,t_0}}{D_k}}{\sum_{k=1}^3 |D_k|^2} \qquad (38)$$

result in a field vector $\mathbf{E}_{t_\perp}$ and a corresponding reflection factor $\rho_{r_i,t_\perp}$ with minimum errors for a given set of $\mathbf{E}_{t_k}$ $(k = 0 \cdots 3)$.

An analogous process orthogonalizes the reference polarizations, and a (transformed) 2×2 reflectance Jones matrix (6) results. By the way, this orthogonalization procedure is also applicable for transmissive devices.

For a sensitivity analysis, we assume the measured reflectances $\rho'_{r_i,t_k}(f)$ to be disturbed by some random errors $n_{ik}(f)$ (noise) of variance σ_n^2

$$\rho'_{r_i,t_k}(f) = \rho_{r_i,t_k}(f) + n_{ik}(f) \quad i,k \in \{0 \cdots 3\}. \qquad (39)$$

The orthogonalized Jones matrix will also be disturbed. If desired it may be multiplied by unitary matrices $[\mathbf{E}_{r_\parallel}, \mathbf{E}_{r_\perp}]$, $[\mathbf{E}_{t_\parallel}, \mathbf{E}_{t_\perp}]^+$ from left and right, respectively, in order to obtain a Jones matrix aligned to the laboratory coordinate system. Its elements

$$\rho'_{i,k}(f) = \rho_{i,k}(f) + \tilde{n}_{ik}(f) \quad i,k \in \{x, y\} \qquad (40)$$

are also disturbed by noise, with variance $\sigma_{\tilde{n}}^2$.
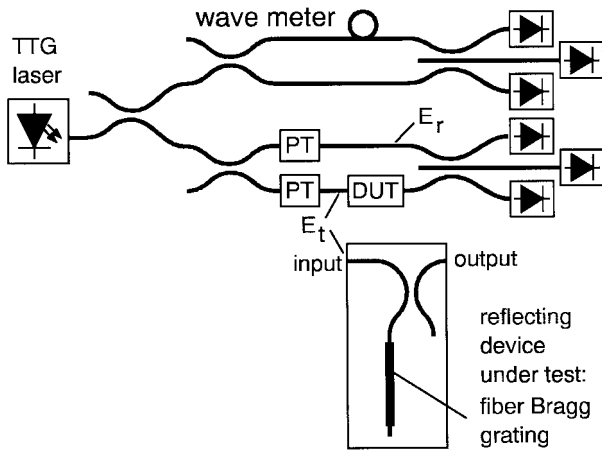
Fig. 3.   Measurement setup, optical network analyzer.

Fig. 4.   UV beams for initial exposure of the grating from the backside (1) and grating fabrication via the phase mask (2).

Extensive, systematic numerical simulations have shown that this variance can be expressed by the approximation

$$\sigma_{\tilde{n}}^2 \approx \frac{1}{2}\sigma_n^2\left(1 + \frac{A}{V_r V_t}\right) \qquad (41)$$

if (38) and its analogon for the reference polarization are applied. The normalized Stokes vector of an electric field vector $E = \begin{bmatrix} E_x & E_y \end{bmatrix}^T$ is given by

$$\mathbf{S} = \frac{1}{|E_x|^2 + |E_y|^2}\begin{bmatrix} |E_x|^2 - |E_y|^2 \\ 2\,\mathrm{Re}(E_x E_y^*) \\ 2\,\mathrm{Im}(E_x E_y^*) \end{bmatrix}. \qquad (42)$$

The normalized Stokes vectors of the 4 reference polarizations form a tetrahedron. Its volume, normalized with respect to that of a regular tetrahedron, is V_r. Its counterpart for the four test polarizations is V_t. Variance $\sigma_{\tilde{n}}^2$ is minimized if the tetrahedrons are regular. The factor A depends on the correlation properties of noise power spectral density and reflectances. In the experiment described in Section IV, the chosen tetrahedron volumina happened to be $V_r = 0.51$, $V_t = 0.028$. For simulated noise with a correlation bandwidth of 3.5 GHz, $\sigma_{\tilde{n}} = 2.3\sigma_n$ was found, which allowed to determine $A = 0.14$ for this case.

IV. EXPERIMENT

The function of an electrical network analyzer may be implemented in the optical domain by interferometric measurement techniques. In our transportable optical network analyzer (Fig. 3) a tunable twin-guide (TTG) laser [17] is used as a tunable laser source. The pump current is left constant. The tuning current introduces a strong decrease of the refractive index of the DFB grating region by the plasma effect, thereby overwhelming the thermal effect which has opposite sign. A set of currently three TTG lasers covers the wavelength range from 1542 to 1556 nm, corresponding to a tuning range of around 4–5 nm for an indivual chip. This is also a typical electronic tuning range of the TTG laser device. Between 0 and 24 mA tuning current, the maximum used in this experiment, the laser linewidth increased from 21 to 45 MHz. The latter value decreases the interferometer contrast to $1/e$ if there is a
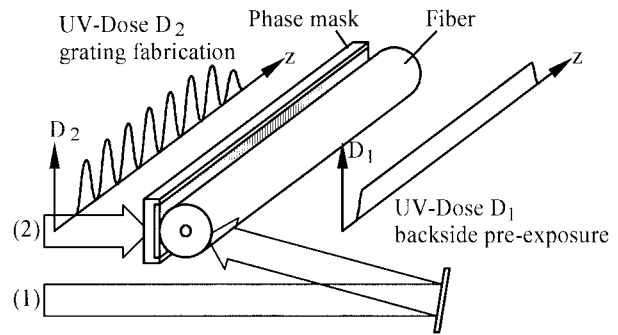
±0.7 m path length difference between the arms. Only a 220-GHz tuning range was used in order to keep the measurement time short. The pump current was 100 mA.

Two variable polarization transformers (PT) control input polarization of the device under test (DUT) and reference polarization, respectively. The polarization transformers consist of two magnetic fiber squeezers each, with $45°$ azimuth angle differences and ~1 ms response times [17]. Additional fixed polarization transformers (fiber loops) were also used. The bottom Mach–Zehnder interferometer (MZI) measures the complex transmission factor of the DUT. A 3×3 coupler [18] with three photodiodes at its outputs is chosen because it allows a more accurate phase measurement than a 2×2 coupler. Real and imaginary parts of a complex grating reflection factor (reflectance) ρ_{ik} are calculated from two linear combinations of the three photodiode currents in the measurement interferometer.

The top MZI has its path length delay adjusted to ~0.5 m. It works as a high-resolution wavelength meter. Corner points of the laser tuning range are checked using an optical spectrum analyzer. A linear frequency dependence of the phase difference is assumed to exist in the MZI's. Higher order frequency dependences, caused by fiber dispersion, are presently neglected. The reading accuracy of the corner points of the laser tuning range results in a center frequency error of the grating and in a scaling error of the z dimension of the grating. The latter can be calibrated at the beginning of a grating fabrication process. For this purpose local reflectivity has to be created by application of UV light at two specific, known z positions of the fiber.

A number of optical isolators (not shown) prevents reflections. Reflecting DUT's such as FBG's are connected by means of an additional coupler (could be replaced by a circulator).

A sampled fiber Bragg grating was fabricated as follows: A hydrogenized fiber (SMF-28) was exposed to UV light from a Kr-F excimer laser (247 nm). An initial backside exposure dose of nominal 3.6 J/mm^2 was applied to compensate for some of the birefringence created by the writing process [5]. Then the front was illuminated through a phase mask (Fig. 4). As the beam moved along the fiber, nominal exposure dose was varied from 0 to 20 J/mm^2 with a 2 mm period, but seventh and eighth period received only 88 and 50% doses, respectively, as in an apodized grating. A sampled grating
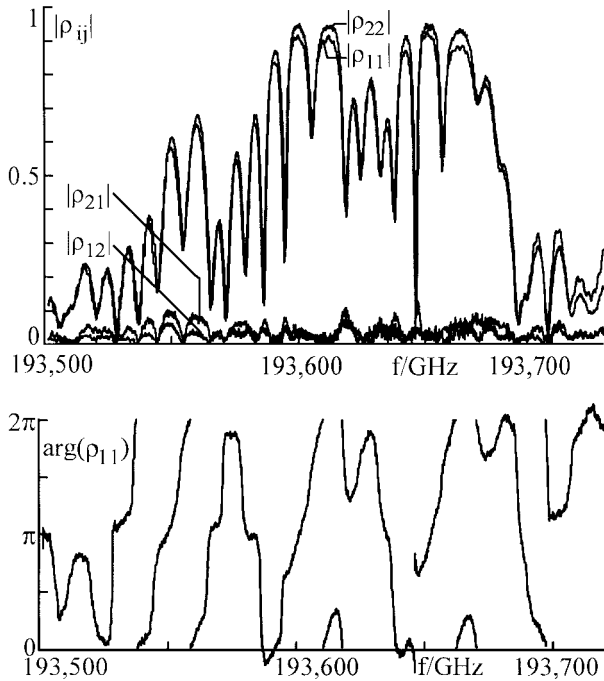
Fig. 5.   Magnitudes of reflectances (top) and, as an example, a phase (bottom).

Fig. 6.   Magnitudes of impulse responses.

with eight spatially equidistant reflecting regions was thus created. Actual may differ from nominal UV dose, and writing efficiency may vary.

The grating was characterized by the network analyzer, using above-described polarization orthogonalization procedure. Reference frequency was $\omega_0 = 2\pi c/1548$ nm, and tuning range was 220 GHz. This corresponds to a spatial resolution of 0.46 mm when calculating the grating structure. Frequency resolution was fine enough to cause us to expect successful characterization of gratings of >1 m length, at least if linewidth data were taken into account.

Reflectance spectra were recorded 12 times for each of the 16 polarization states, with sampled frequency points and frequency resolutions increasing by a factor of two each time. The coarse sweeps take little time and are affected by drift only to a small extent. Their data is used to correct phase drifts in the sweeps with finer resolution. Most of the thermal interferometer drift is thereby eliminated.

Fig. 5 shows the four orthogonalized reflectance magnitudes $|\rho_{ik}(f)|$ and, as an example of measured phases, $\arg(\rho_{11}(f))$ after removal of a 136 ps group delay. The near-periodic behavior of the magnitudes (many maxima and minima) indicates Fabry–Perot resonances, as expected for a sampled grating. A spectral superstructure with $\sim$50 GHz periodity is caused by the 2 mm distance between adjacent reflecting regions. Some dichroism is visible.

An Inverse fast Fourier transform (FFT) yields the complex impulse response matrix $\mathbf{U}(t) = \mathbf{U}(0, t)$. Magnitude plots (Fig. 6) reveal again that the grating is sampled. More than nine impulses are produced by the eight reflecting grating regions. Discrepancies between the impulse response and the grating structure are caused by multiple reflections inside the grating. Furthermore, the impulse response shows a falling
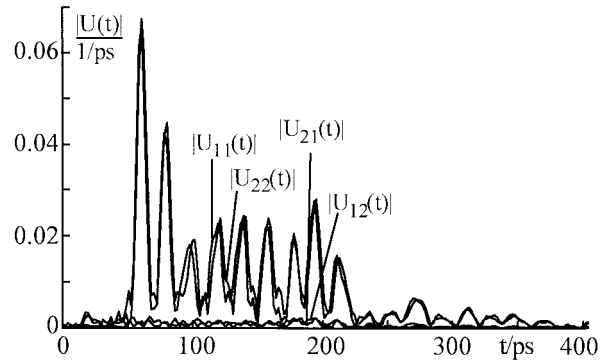
tendency of the impulse heights which is caused by the fading of the initial forward-propagating impulse due to previous reflections. Phases are not shown for simplicity.

The grating structure was derived from the impulse response matrix in terms of the eight unknowns of local grating reflectivity κ and birefringence β, assuming $\gamma \equiv 0$. It was possible to choose input and reference polarizations $\mathbf{E}_t$ and $\mathbf{E}_r$ such that $|\Delta n_{pp12}|$ and $|\Delta n_{12}|$ nearly vanish. In this coordinate system reflectivity eigenmodes are nearly linear polarizations with 0 and 90° azimuths. The eight reflecting regions are clearly identified [Fig. 7(a)]. Some reflection dichroism is present. Smaller than expected reflectivities, as observed in the middle of the grating, may be due to a gap between phase mask and fiber. We expect they could be improved by additional UV light. Grating phase ϕ and birefringence matrix β can only be determined meaningfully for $z = 8 \cdots 24$ mm where nonzero reflectivity exists.

If the grating had a constant physical pitch and no mask-induced stitch errors we could replace the grating phase $\phi(z)$ in (2) by a term proportional to the integral over a global mean refractive index deviation $\Delta n(z)$, as can be seen from comparison with (1)

$$\phi(z) = -2(\omega_0/c) \int \Delta n(z) \, dz. \tag{43}$$

Grating phase varies strongly [Fig. 7(b)]. There are oscillations with a 2 mm period. Inside the reflecting regions (bursts) ϕ is falling, between them it is rising. The calculated refractive index deviation $\Delta n(z) = -(d\phi/dz)c/(2\omega_0)$ was found to be more positive by $\sim 3 \cdots 7 \cdot 10^{-4}$ inside the bursts than outside, with substantial variations between different bursts. This figure is believed to be the mean refractive index increase caused by the UV exposure inside the reflecting regions. Comparison of the measured refractive index modulation depths $\Delta n_{ppik}(z)$ to twice the mean refractive index increase also allows to roughly estimate the UV interference pattern contrast in a burst.

Even if ϕ is smoothed over 2 mm periods an irregular pattern persists which shows that the phase mask is of bad quality. However, the optical path lengths between reflecting regions are thereby revealed. This should allow for compensation of stitch errors of the phase mask. To this purpose UV light would have to be applied through a dithered phase mask or in absence of a phase mask so that mainly the mean refractive index but not the refractive index difference should increase.
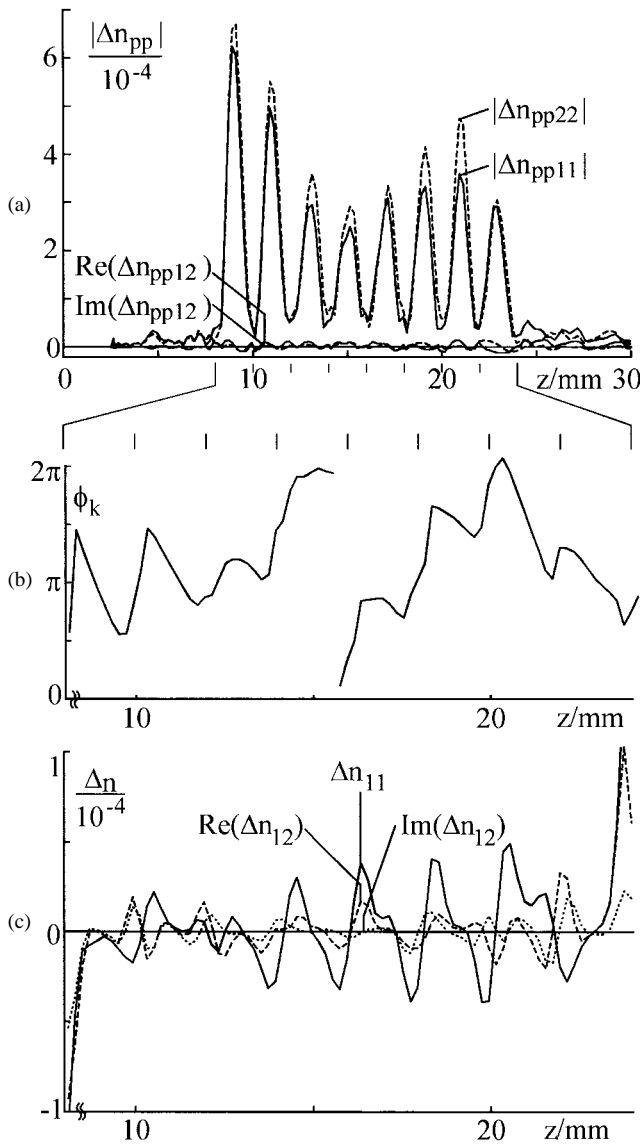
Fig. 7. Experimentally determined structure parameters [(a) elements of κ, (b) grating phase ϕ, and (c) elements of β] of a sampled grating.

Fig. 8. One-dimensional simplification: Scalar algorithm yields results similar to Fig. 7(a). Connecting either "front" or "back" of the grating to the interferometer makes little difference.

Birefringence terms Δn_{11} and Δn_{12} [Fig. 7(c)] have 2 mm periods like the reflecting regions. This may be due to periodic front and uniform backside UV illumination, but further investigation is required. Obtained birefringence data might be used to improve the UV exposure process.

Additional, though weak structures outside the reflecting region [Fig. 7(a)] suggest measurement accuracy could still be improved. In a test, polarizations were adjusted for maximum reflectance. Overall measurement time is thereby greatly reduced. Equations were simplified for 1×1 complex scalars and solved, with Δn_{pp}, ϕ as results. And indeed, in Fig. 8, bottom trace, Δn_{pp} pre- and postcursors outside $z = 8 \cdots 24$ mm are better suppressed than in Fig. 7(a). The estimated measurement accuracy is roughly $\Delta n_{pp} = 10^{-5}$. In another measurement the grating was reversed. "Forward" and "backward" results agree very well. The discrepancies allowed us to estimate the cumulative grating loss as 0.6 dB. Other discrepancies between the traces in Fig. 8 could be due to polarization

sensitivity, and uncompensated interferometer drift. It may bee seen that the postcursors ($z < 8$ mm in top, $z > 20$ mm in bottom trace) are stronger than the respective precursors ($z > 20$ mm in top, $z < 8$ mm in bottom trace). The reason for this is error propagation in the inverse scattering algorithm.

Uncompensated interferometer drift is indeed assumed to be the main error source, although most of it is eliminated by the described countermeasure. Future work will therefore aim at minimizing the measurement time. Zero-bias operation of the photodiodes presently requires 12 sweeps (with increasing resolutions) per spectrum, and this takes $\sim$10 min. The lower accuracy of the polarization-resolved data (dichroic coupling and birefringence in Fig. 7) with respect to scalar data (refractive index difference in Fig. 8 and grating phase) can be understood from the fact that 16 such spectra have to be recorded.

A much smaller measurement time should also allow us to increase frequency span and, as a consequence, spatial resolution.

In contrast, based on previous experience we do not think that polarization drift in the interferometers played a significant role.

V. SUMMARY

We have measured the complete complex 2×2 Jones matrix of a fiber Bragg grating, using an optical network analyzer. An orthogonalization procedure eliminates the need for accurate polarization transformers; they just need to operate reproducibly. Local dichroic reflectivity and birefringence of the FBG have been derived from this data. The isotropic structure has also been obtained, in less time and with higher accuracy. Agreement between grating fabrication process, scalar, and matrix structure data has been found. Results may be used to optimize refractive index modulation depth, phase mask pitch, and UV illumination process.

ACKNOWLEDGMENT

The authors would like to thank S. Hinz for his contribution to this work.

REFERENCES

[1] K. O. Hill, B. Malo, F. Bilodeau, D. C. Johnson, and J. Albert, "Bragg gratings fabricated in monomode photosensitive optical fiber by UV exposure through a phase mask," *Appl. Phys. Lett.*, vol. 62, pp. 1035–1037, 1993.

[2] R. Kashyap, A. Ellis, D. Malyon, H. G. Froehlich, A. Swanton, and D. J. Armes, "Eight wavelength ×10 Gb/s simultaneous dispersion compensation over 100 km single-mode fiber using a single 10 nanometer bandwidth, 1.3 meter long, super-step-chirped fiber Bragg grating with a continuous delay of 13.5 nanoseconds," in *Proc. ECOC'96*, ThB.3.2, vol. 5, pp. 7–10.

[3] M. J. Cole, H. Geiger, R. I. Laming, S. Y. Set, M. N. Zervas, W. H. Loh, and V. Gusmeroli, "Continuously chirped, broadband dispersion-compensating fiber gratings in a 10 Gbit/s 110 km standard fiber link," in *Proc. ECOC'96*, ThB.3.5, vol. 5, pp. 19–22.

[4] F. Ouellette, P. A. Krug, T. Stephens, G. Dhosi, and B. Eggleton, "Broadband and WDM dispersion compensation using chirped sampled fiber Bragg gratings," *Electron. Lett.*, vol. 31, no. 11, pp. 899–901, 1995.

[5] A. M. Vengsarkar, Q. Zhong, D. Inniss, W. A. Reed, P. J. Lemaire, and S. G. Kosinski, "Birefringence reduction in side-written photoinduced fiber devices by a dual/circumferential exposure method," in *Proc. OFC'94*, PD5.

[6] K. Sano, T. Kudou, and T. Ozeki, "Simultaneous measurement of group delay time dispersion and polarization mode dispersion," in *Proc. 22nd ECOC*, Oslo, Norway, vol. 2, pp. 253–256, TuP.09, Sept. 15–19, 1996.

[7] P. Lambelet, P. Y. Fonjallaz, H. G. Limberger, R. P. Salathé, C. Zimmer, and H. H. Gilgen, "Bragg grating characterization by optical low-coherence reflectometry," *IEEE Photon. Technonol. Lett.*, vol. 5, pp. 565–567, 1993.

[8] E. Brinkmeyer, "Simple algorithm for reconstructing fiber gratings from reflectometric data," *Opt. Lett.*, vol. 20, pp. 810–812, 1995.

[9] S. Barcelos, M. N. Zervas, R. I. Laming, D. N. Payne, L. Reekie, J. A. Tucknott, R. Kashyap, P. F. McKee, F. Sladen, and B. Wojciechowicz, "Dispersion measurements of chirped fiber gratings," in *Proc. ECOC'95*, Mo.A.3.4, pp. 35–38.

[10] D. Sandel and R. Noé, "Chirped fiber bragg gratings for optical dispersion compensation: How to improve their fabrication accuracy," in *Proc. ECOC'96*, TuP.04, vol. 2, pp. 233–236.

[11] Y. Namihira and J. Maeda, "Comparison of various polarization mode dispersion measurement methods in optical fibers," *Electron. Lett.*, vol. 28, pp. 2265–2266, 1992.

[12] B. L. Heffner, "Automated measurement of polarization mode dispersion using jones matrix eigenanalysis," *IEEE Photon. Technol. Lett.*, vol. 4, pp. 1066–1069, 1992.

[13] Y. Namihira, K. Nakajima, and T. Kawazawa, "Fully automated interfero-metric PMD measurements for active EDFA, fiber optic components and optical fibers," *Electron. Lett.*, vol. 29, pp. 1649–1651, 1993.

[14] D. Sandel and R. Noé, "Optical network analyzer applied for fiber Bragg grating characterization," in *Proc. IOOC/ECOC'97*, WE3, Edinburgh, U.K., Sept. 22–25, 1997.

[15] R. Ulrich and A. Simon, "Polarization optics of twisted single mode fibers," *Appl. Opt.*, vol. 18, pp. 2241–2251, 1979.

[16] S. Illek, W. Thulke, C. Schanen, and M.-C. Amann, "Over 7 nm (875 GHz) continuous wavelength tuning by tunable twin-guide (TTG) laser diode," *Electron. Lett.*, vol. 26, pp. 46–47, 1990.

[17] R. Noé, H. Heidrich, and D. Hoffmann, "Endless polarization control systems for coherent optics," *J. Lightwave Technol.*, vol. 6, pp. 1199–1207, July 1988.

[18] R. G. Priest, "Analysis of fiber interferometer utilizing 3 × 3 fiber coupler," *IEEE J. Quantum Electron.*, vol. QE-18, pp. 1601–1603, Oct. 1982.

David Sandel was born on December 20, 1966, in Wangen/Allgäu, Germany. He received the Dipl.-Ing. degree from the Technische Hochschule Karlsruhe, Germany, in 1992 and the Dr.-Ing. degree on fiber Bragg gratings from the University of Paderborn, Germany, in 1997.

In 1992, he joined the Optical Communications and High-Frequency Engineering in the Department of Electrical Engineering at the University of Paderborn. His research interests now concentrate on polarization dispersion compensation.

Reinhold Noé was born in Darmstadt, Germany, 1960. He received the Dipl.-Ing. and Dr.-Ing. degrees in electrical engineering from the Technical University of Munich, Germany, in 1984 and 1987, respectively. His Ph.D. dissertation was on endless polarization control.

He spent a Postdoctoral year at Bellcore, Red Bank, NJ. In 1988, he joined the Siemens Research Laboratories in Munich, working on coherent optical systems. Since 1992, he has been the Chair of Optical Communications and High-Frequency Engineering in the Department of Electrical Engineering at the University of Paderborn, Germany. His interests are in the area of optical communications, where he is working on polarization mode dispersion compensation, fiber Bragg gratings, and applications of lithium niobate devices.

G. Heise, photograph and biography not available at the time of publication.

B. Borchert, photograph and biography not available at the time of publication.